Colored dissolved organic matter absorption at global scale from ocean color radiometry observation: Spatio-temporal variability and contribution to the absorption budget

Ana Gabriela Bonelli, Vincent Vantrepotte, Daniel Schaffer Ferreira Jorge, Julien Demaria, David Dessailly, Antoine Mangin, Odile Fanton d'Andon, Ewa Kwiatkowska, Cédric Jamet, Hubert Loisel

Remote Sensing of Environment 265 (2021) 112637

Contents lists available at ScienceDirect

Remote Sensing of Environment

journal homepage: www.elsevier.com/locate/rse

Colored dissolved organic matter absorption at global scale from ocean color radiometry observation: Spatio-temporal variability and contribution to the absorption budget

Ana Gabriela Bonelli [a,b,*], Vincent Vantrepotte [a], Daniel Schaffer Ferreira Jorge [a], Julien Demaria [b], Cédric Jamet [a], David Dessailly [a], Antoine Mangin [b], Odile Fanton d'Andon [b], Ewa Kwiatkowska [c], Hubert Loisel [a]

[a] Univ. Littoral Côte d'Opale, Univ. Lille, CNRS, UMR 8187, LOG, Laboratoire d'Océanologie et de Géosciences, F 62930 Wimereux, France
[b] ACRI-ST, 260 Route du Pin Montard, Sophia-Antipolis, 06410 Biot, France
[c] EUMETSAT, Darmstadt, Germany

ARTICLE INFO

Editor: Dr. Menghua Wang

Keywords:
Colored dissolved organic matter
$a_{cdom}(443)$
Ocean color remote sensing
Open ocean

ABSTRACT

A semi-analytical model (CDOM-KD2) based on the light vertical attenuation coefficient ($K_d(\lambda)$) has been developed for estimating the absorption by colored dissolved organic matter, $a_{cdom}(443)$, from ocean color remote sensing at global scale. The performance of this new inversion model together with that of former models by Shanmugam (2011) (S2011), Chen et al. (2017) (C2017) and Aurin et al. (2018) (A2018) was evaluated from in situ and matchup validation data sets gathering worldwide distributed samples. An overall consistency in the $a_{cdom}(443)$ estimated from S2011, C2017 and CDOM-KD2 models with a slightly better performance of the latter method was observed (MAPD of 27.42% and 30.85% for open ocean with in situ and satellite data, respectively), emphasizing the possible specific assessment of $a_{cdom}(443)$ dynamics from satellite remote sensing over the global ocean including the most oligotrophic waters. At 443 nm the global average relative contribution of $a_{cdom}(443)$ to the absorption by colored detrital matter, $a_{cdm}(443)$ is of 61% ± 14%, while the contribution of $a_{cdom}(443)$ to the non-water absorption, $a_{nw}(443)$, is of 35% ± 26%. Strong spatial disparities are however observed for both $a_{cdom}(443)$ temporal dynamics and relative contribution in the absorption budget. A decoupling is observed between $a_{cdom}(443)$ and particulate detrital (i.e. non-living) matter and phytoplankton in the gyre areas where a low temporal variability is globally observed. This is contrasting with water masses influenced by terrestrial inputs as well as in equatorial and subtropical areas impacted by main oceanic currents where CDOM loads and $a_{cdom}(443)$ contribution in the water absorption budget are more variable.

1. Introduction

The Colored dissolved organic matter (CDOM), also known as gelbstoff, gilvin and yellow substance, is the colored fraction of the total dissolved organic material (DOM) (Coble, 2007). Although it represents a small part of the total DOM in the open sea (Nelson et al., 1998, 2010; Nelson and Siegel, 2002; Siegel et al., 2002), CDOM plays a significant role in aquatic photochemistry and photobiology, interfering in various biogeochemical cycles as it absorbs light over a broad spectral range covering visible and UV domains (Aurin et al., 2018; Blough and Del Vecchio, 2002; Coble, 2007; Kieber et al., 1996; Toole et al., 2006). The absorption of CDOM (a_{cdom}) used to estimate CDOM concentration in water (Coble et al., 2004), represents the optical proxy for assessing Dissolved Organic Carbon concentration in coastal waters (Del Castillo and Miller, 2008; Fichot and Benner, 2011; Mannino et al., 2008; Vantrepotte et al., 2015). The composition of CDOM is very complex and diverse, depending on its origin, labile fraction, age, and whether it has transitioned from fresh waters to marine environment. Coastal waters generally present high concentrations of CDOM, mainly of terrestrial origin, introduced to the oceanic system through river discharge and

* Corresponding author at: Univ. Littoral Côte d'Opale, Univ. Lille, CNRS, UMR 8187, LOG, Laboratoire d'Océanologie et de Géosciences, F 62930 Wimereux, France.
E-mail addresses: agbonelli@gmail.com (A.G. Bonelli), oha@acri-st.fr (O. Fanton d'Andon), ewa.kwiatkowska@eumetsat.int (E. Kwiatkowska), hubert.loisel@univ-littoral.fr (H. Loisel).

https://doi.org/10.1016/j.rse.2021.112637
Received 18 January 2021; Received in revised form 2 August 2021; Accepted 3 August 2021
Available online 25 August 2021

land washing (Coble et al., 1998; Tzortziou et al., 2015). For this reason, $a_{cdom}(\lambda)$ can be used as a good tracer of inland waters dispersion in coastal areas (Fichot and Benner, 2012). In contrast to coastal waters, CDOM in the open ocean is mainly of marine origin; being produced in the euphotic zone and/or advected by horizontal and vertical currents (Coble, 2007; Nelson and Siegel, 2013; Organelli et al., 2014). In this type of water, and out of areas affected by advection of coastal waters, CDOM is generally considered a residual product of phytoplankton and other organic particles. This production is related to a variety of biological processes including viral lysis, bacterial degradation, excretion by phytoplankton and phytoplankton grazing by zooplankton (Bricaud et al., 1981; Coble, 2007; Nelson et al., 1998, 2010; Nelson and Siegel, 2002; Prieur and Sathyendranath, 1981). CDOM sink processes are mainly related to microbial consumption and photooxidation which explain about 40% (Carlson and Ducklow, 1996) and 50% to 75% (Bricaud et al., 1981; Mannino et al., 2008) of the reduction of CDOM, respectively, thus strongly driving the net CDOM balance in the open ocean (Siegel et al., 2002; Nelson et al., 2007; Coble, 2007). The dynamic of CDOM in open ocean waters is strongly dependent on the coupling between physical and biogeochemical processes which rely on forcing parameters such as the light availability and vertical mixing. The great diversity of processes controlling a_{cdom} variability make its dynamics over the open ocean still not well characterized. Besides the necessity to improve our knowledge on the oceanic spatio-temporal distribution of $a_{cdom}(\lambda)$, the strong absorption by CDOM in the blue spectral domain interferes with estimates of chlorophyll-a concentration, *Chl-a*, from ocean color observation (Carder et al., 1991; Loisel et al., 2010; Siegel et al., 2005a, 2005b, 2013).

The similar spectral behaviors between $a_{cdom}(\lambda)$ and the absorption coefficient by non-algal particles, $a_{nap}(\lambda)$, makes these two absorption coefficients difficult to distinguish from ocean color inverse algorithms. For this reason, the ocean color community has historically focused on the development of inverse algorithms to assess the colored detrital matter absorption coefficient, $a_{cdm}(\lambda)$, which combines the contributions of non-algal particles and CDOM (e.g. Boss and Roesler, 2006; Ciotti and Bricaud, 2006; Lee et al., 2002; Maritorena et al., 2002). In coastal waters, however, where the concentration of CDOM is greater and the source and sink processes controlling the variability of a_{nap} and a_{cdom} are strongly decoupled, various empirical and semi-analytical approaches have successfully been developed to specifically assess $a_{cdom}(\lambda)$ (e.g. Cao et al., 2018; Loisel et al., 2014; Mannino et al., 2008). Over open ocean waters, where CDOM is present in a much lower concentration than in coastal waters, the first Ocean Color Radiometry (OCR) algorithm dedicated to the estimation of $a_{cdom}(\lambda)$ was based on the use of variable $a_{cdom}(443)$ vs *Chl-a* relationships (Morel and Gentili, 2009). However, as mentioned by the latter authors, this algorithm only provides a relative estimate of $a_{cdom}(\lambda)$, since it is calculated "in reference to a standard Chlorophyll-a content". More recently, purely empirical approaches based on blue-to-green reflectance ratios (Shanmugam, 2011), or multi linear regression (MLR) between $a_{cdom}(\lambda)$ and $R_{rs}(\lambda)$ at different wavelengths (Aurin et al., 2018) have been proposed to assess $a_{cdom}(\lambda)$ from ocean color observation. Based on matchup between satellite GSM-derived $a_{cdm}(443)$ values (Maritorena et al., 2002) and in situ $a_{cdom}(\lambda)$ measurements a semi-analytical approach has also been proposed by Swan et al. (2013) to assess $a_{cdom}(\lambda)$ from $a_{cdm}(443)$. Very recently, a semi-analytical approach involving other inherent optical properties (IOPs) has been developed to assess $a_{cdom}(443)$ in coastal and open ocean water (Chen et al., 2017).

This study emerged in this context and aims at i) proposing the best approach to adequately assess $a_{cdom}(443)$ over oceanic areas, ii) assessing the $a_{cdom}(443)$ variability with regards to the chlorophyll-a concentration and $a_{cdm}(443)$, and iii) quantifying the contribution of $a_{cdom}(443)$ to $a_{cdm}(443)$ and the non-water absorption coefficients, $a_{nw}(443)$, over the global ocean. For that purpose, the performance of different algorithms, including a new one and three previously published algorithms, is evaluated using a large set of in situ and matchup data points. The description of these in situ and satellite data are first provided. The different selected algorithms are then presented, and the adaptation of a previously published algorithm dedicated to the estimation of $a_{cdom}(412)$ in coastal waters is described. The description of the $a_{cdom}(443)$ spatio-temporal patterns, as well as of its relative contribution to $a_{cdm}(443)$ and $a_{nw}(443)$ are then provided.

2. Materials and methods

2.1. Datasets description

2.1.1. Optical typology

In order to evaluate the performance of the different $a_{cdom}(443)$ inversion models considered according to the optical water type characteristics, each sample available was associated with the 16 optical classes defined by Mélin and Vantrepotte (2015) defined from a global coastal waters classification of the R_{rs} spectral shape (normalized reflectance spectra). The 16 classes defined by the latter authors cover a large part of the optical diversity of marine waters including oceanic waters, to the exception of the most oligotrophic gyre environment. A specific additional class numbered as 17, has been therefore added following the methodology described in Jorge et al. (2021). Data belonging to classes 1 and 2 can be considered as representing turbid water masses strongly impacted by terrestrial inputs. In contrast, samples associated with classes 9 to 17 correspond to waters where the reflectance spectra are well represented by the Case 1 reflectance model by Morel and Maritorena (2001), while samples for classes 3 to 8 are more likely related to diverse types of Case 2 waters where the spectral shape is increasingly different from the Case 1 modeled spectra.

2.1.2. In situ and matchup data sets used for validation

Three different datasets were defined for the development, validation and inter-comparison exercises presented in this study. The first dataset (DS1) corresponds to the synthetic ocean color dataset developed by the International Ocean Color Coordinating Group (IOCCG) working group dedicated to inverse algorithm development (IOCCG, 2006). This dataset gathers 500 data points of inherent optical properties (IOPs) and remote sensing reflectance, $R_{rs}(\lambda)$, computed from radiative transfer simulations every 3 nm from 400 to 700 nm for each IOPs combination. The $a_{cdom}(443)$ values for the whole DS1 dataset range between 0.0025 m^{-1} and 2.37 m^{-1}, with a median value of 0.12 m^{-1} (Fig. 1 a). This data set is used for the development of the new algorithm, hereafter referred as CDOM-KD2. The evaluation of the relative performances of the different considered algorithms has been carried out using an in situ validation dataset (DS2) and a matchup dataset (DS3).

The DS2 (Fig. 1 d, e, f) data set includes 1001 in situ $R_{rs}(\lambda)$ and $a_{cdom}(443)$ measurements distributed worldwide (Fig. 1 j). It gathers data collected from diverse cruises previously presented in Loisel et al. (2018), and other additional data collected within the NOMAD (Werdell and Bailey, 2005) and Plumes and Blooms (https://seabass.gsfc.nasa.gov/experiment/Plumes_and_Blooms) projects not included in Loisel et al. (2018). The $a_{cdom}(443)$ range of variability in DS2 is [0.002; 7.84] m^{-1}, with a median value of 0.094 m^{-1}.

The DS3 matchup dataset was built from two distinct data sets. First, the GlobColour daily merged L3 Ocean Color products at 4 km^2 of spatial resolution (http://www.globcolour.info/CDR_Docs/GlobCOLOUR_PUG.pdf) were matched with the in situ GOCAD (Aurin et al., 2018) data set and covers the September 1997–August 2012 time period. The matchups were computed following the MERMAID tools protocol (http://mermaid.acri.fr/dataproto/dataproto.php) which is based on the NASA Ocean Color protocol (Bailey and Wang, 2001). In practice, daily matchups (with a 3-h time window) were produced using a 3 × 3 pixel window, in which the coefficient of variation of $R_{rs}(\lambda)$ needs to be below 0.15 while the number of valid pixels needs to be above 50% (implying a minimum of 5 valid pixels). The second matchup data set is the NOMAD matchup dataset (Werdell and Bailey, 2005) based only on

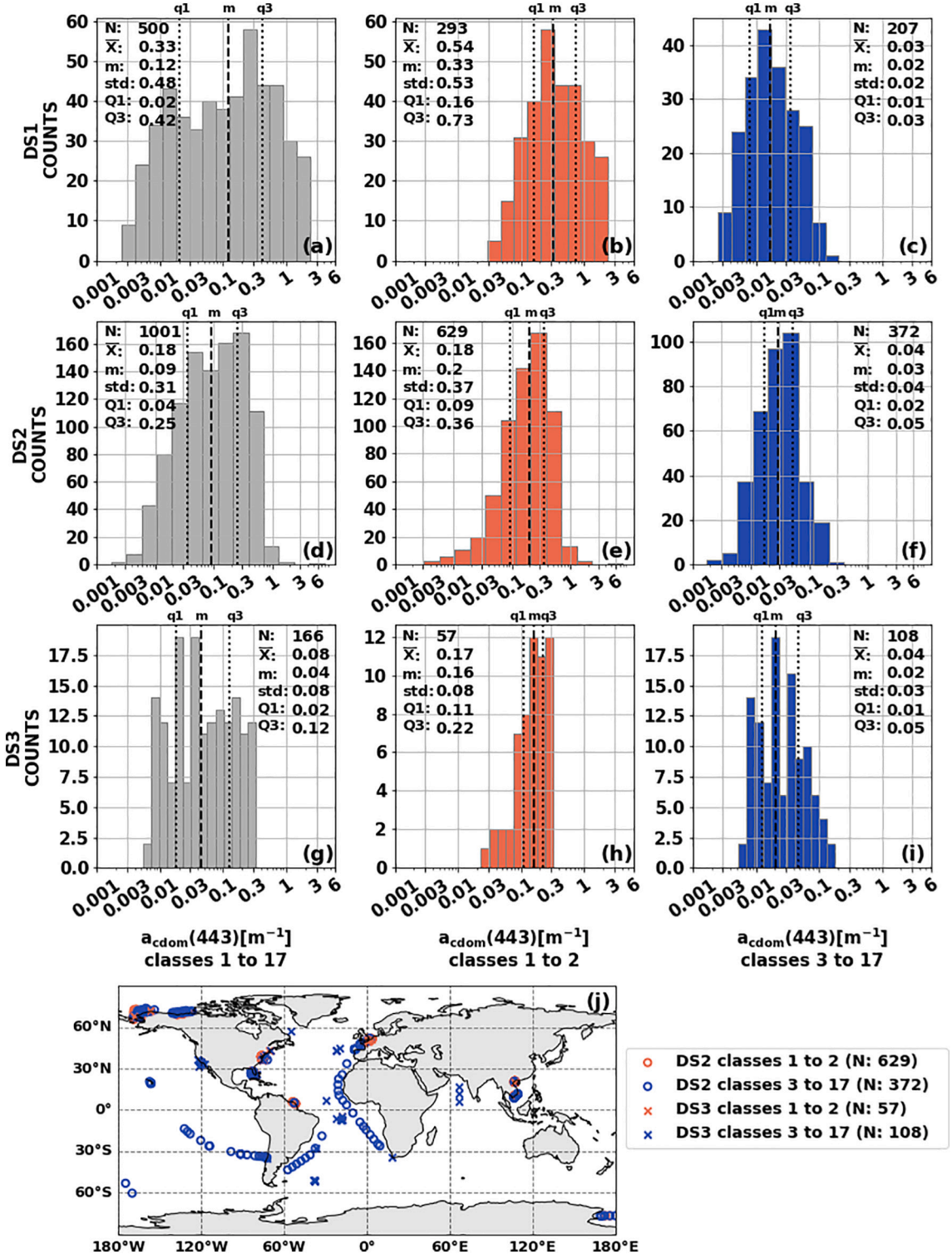

Fig. 1. From top to bottom, $a_{cdom}(443)$ absolute frequency distribution histograms for DS1 (a, b, c), DS2 (d, e, f) and DS3 (g, h, i) datasets and spatial distribution of DS2 and DS3 (j). The complete datasets are represented in gray, classes 1 and 2 subsets are in red, and classes 3 to 17 in blue. N, $\overline{X}$, m, std., q1, q3 correspond to the number of data points, mean, median, standard deviation and first and third quantiles values, respectively. (For interpretation of the references to color in this figure legend, the reader is referred to the web version of this article.)

SeaWiFS observations and gathering data collected between October 1997 and March 1999. Thus, DS3 corresponds to the merging of GOCAD and NOMAD matchup data sets, gathering a total of 399 stations. To limit the impact of the propagation of $R_{rs}(\lambda)$ errors, due to imperfect atmospheric corrections on the $a_{cdom}(443)$ retrieval accuracy, an additional condition was applied on the selection of the matchup data points for the two matchup data sets. In practice, a matchup data was considered invalid if, for any visible wavelengths used in the algorithms, the absolute difference between satellite $R_{rs}(\lambda)$ and in situ $R_{rs}(\lambda)$ was greater than 0.75 * in situ $R_{rs}(\lambda)$ (Fig. 2). Among the initial 399 matchups data, 166 points were kept after applying the latter quality criterion. The $a_{cdom}(443)$ range of variability in DS3 is [0.0052; 0.33] m^{-1}, with a

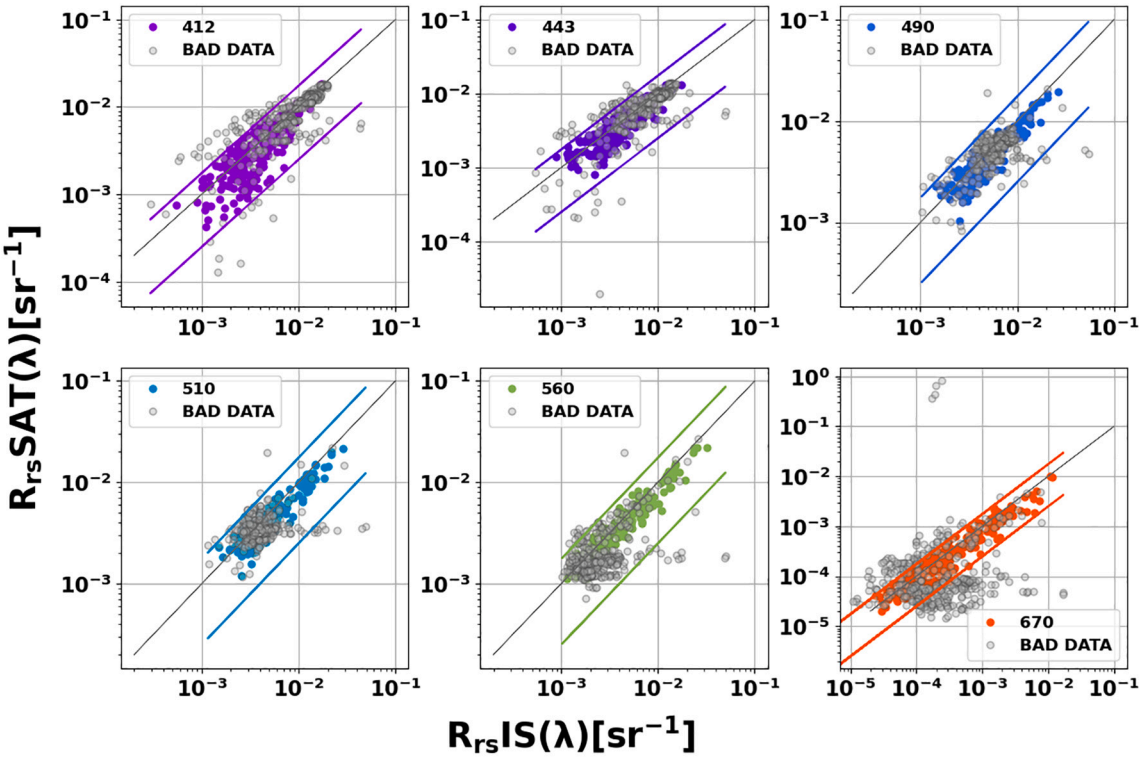

Fig. 2. Satellite R_{rs} (R_{rs} SAT) vs in situ R_{rs} (R_{rs} IS) from DS3 at (a) 412, (b) 443, (c) 490, (d) 510, (e) 560 and (f) 670 nm. Black solid line represents the 1:1 line, colored solid lines are the threshold limit, where $|R_{rs}$ SAT- R_{rs} IS$| > R_{rs}$ IS * 0.75. Gray circles represent the data points for which any of the bands overcomes the settled threshold. These data points where labeled as outliers and not further considered in the analysis.

median value of 0.08 m^{-1}. Even if DS3 time period (23rd April 2002 to 13th April 2012) covers the last ocean color sensor missions which have been recently launched, OLCI A and B, matchup for these sensors are unfortunately not available in our present data base of $a_{cdom}(443)$ in situ measurements.

2.1.3. Satellite Data used for global CDOM spatio-temporal variability

The global spatio-temporal dynamics of satellite derived $a_{cdom}(443)$ was assessed from GlobColour L3 merged $R_{rs}(\lambda)$ data.

The GlobColour L3 merged data include satellite observations from SeaWiFS, MERIS, MODIS Aqua and VIIRS NPP sensors. These merged products ($R_{rs}(\lambda)$, *Chl-a*, and $a_{cdm}(\lambda)$) are generated by simple averaging or weighted averaging, depending on the conditions (water types, region, glint/aerosol conditions, etc.). Both *Chl-a*, and $a_{cdm}(\lambda)$ are estimated by the GSM model (Maritorena and Siegel, 2005). Global maps and the time series extraction were produced with GlobColour L3 merged 25 km resolution and 8 days composite data from 23rd April 2002 to 13th April 2012.

2.2. Statistical indicators

The performance of the $a_{cdom}(443)$ inversion models was evaluated from a graphical comparison sustained with quantitative statistical metrics including: the root mean the square deviation (RMSD, Eq. (1)), the median ratio (MR, Eq. (2)), the median absolute percent difference (MAPD, Eq. (3)) and the Pearson correlation coefficient (r).

$$RMSD = \sqrt{\frac{\sum_{i=1}^{N}(yi - xi)^2}{N}} \quad (1)$$

$$\mathrm{MR} = \frac{median(yi)}{median(xi)} \quad (2)$$

$$MAPD = median\sum_{i=1}^{N}\frac{|yi - xi|}{xi} * 100 \quad (3)$$

where y_i and x_i are the estimated and the in-situ values, respectively.

The MAPD has been calculated considering the median of the individual absolute percent differences between the modeled and measured data instead of the mean to minimize the impact of potential outliers (Loisel et al., 2018).

These statistical parameters were summarized in radar plots where smaller polygon areas indicate improved model performance.

2.3. Models description

In the present paper, four different models are evaluated for estimating $a_{cdom}(443)$ from OCR. These general models, which are based on different assumptions, include two empirical methods recently defined by Aurin et al. (2018) and Shanmugam (2011), and two semi-analytical approaches proposed by Chen et al. (2017) and Loisel et al. (2014). This latter model, dedicated to the estimation of $a_{cdom}(412)$, is here modified and improved to assess $a_{cdom}(443)$.

2.3.1. Aurin et al. (2018)

Aurin et al. (2018) (further referred to as A2018) recently developed an empirical model for estimating $a_{cdom}(\lambda)$ at global scale. This model is based on a multiple linear regression (MLR) between the natural logarithm of $R_{rs}(\lambda)$ at four different visible wavelengths and the natural logarithm of $a_{cdom}(\lambda)$. It can be described as follows:

$$ln(a_{cdom}(\lambda)) = \begin{pmatrix} \beta 0 + \beta 1 * ln(R_{rs}(\lambda_1)) + \beta 2 * ln(R_{rs}(\lambda_2)) \\ + \beta 3 * ln(R_{rs}(\lambda_3)) + \beta 4 * ln(R_{rs}(\lambda_4)) \end{pmatrix} \quad (4)$$

where λ_1 to λ_4 are the sensor-specific wavelengths (i.e., 443, 488, 531, and 547 nm for MODIS, 443, 490, 510, and 555 nm for SeaWiFS). $\beta 0$ to

β4 are the regression coefficients for estimating $a_{cdom}(443)$ (here β0 = −6.41; β1 = −0.743; β2 = −0.145; β3 = −0.367; and β4 = 0.547).

Although the authors specify that the version of the model developed for MODIS data has a significantly better performance ($r^2 = 0.85$), in this work, only the SeaWiFS version of the model has been considered ($r^2 = 0.33$) in order to perform a fair inter-comparison exercise between models which use exactly the same $R_{rs}(\lambda)$ as input parameters.

Considering that empirical models such as MLR approaches are highly dependent to the datasets used for their development, the applicability of this model is expected to be limited.

2.3.2. Chen et al. (2017)

Chen et al. (2017) (further referred to as C2017) recently developed a semi-analytical model aiming at estimating $a_{cdom}(443)$ at global scale from the particulate backscattering coefficients, $b_{bp}(443)$, and the absorption coefficients of phytoplankton, $a_{phy}(443)$, and colored detrital matter, $a_{cdm}(443)$, as follows:

$$a_{cdom}(443) = \chi^* a_{cdm}(443) + \gamma^* b_{bp}(555) + \kappa^* a_{phy}(443) \quad (5)$$

where χ, γ and κ are three independent empirical parameters covarying with the water optical properties estimated from the NQAA algorithm (Chen et al., 2016). χ is a function of the a(λ)-based triangle area index of the total absorption coefficient (TAI). The a(λ)-based TAI is defined as follows:

$$TAI = a(\lambda) - \left(\frac{555-490}{555-443}\right)^* a(\lambda_0) - \left(\frac{490-443}{555-443}\right)^* a(\lambda_2) \quad (6)$$

where a is the total absorption coefficient calculated by NQAA (Chen et al., 2016).

Chen et al. (2016) documented, based on SeaWiFS satellite data validation exercise, an overall good performance of their model for estimating $a_{cdom}(443)$ over values ranging from 0.001 to 1.116 m^{-1}. The latter authors further emphasized that this model is able to solve errors in the $a_{cdom}(443)$ estimates induced by the backscattering signal of particles but also underlined the slight underestimation of $a_{cdom}(443)$ towards the lowest end-member values ($a_{cdom}(443) < 0.005$ m^{-1}).

2.3.3. Shanmugam (2011)

This model, developed for coastal and ocean waters, uses two slope parameters to describe $a_{cdom}(\lambda)$ in the UV and visible spectral domain as follows:

$$a_{cdom}(\lambda) = a_{cdom}(350)^* e^{\left(-S(\lambda-350)-\gamma^0\right)} \quad (7)$$

where $a_{cdom}(350)$ is estimated from the blue to green reflectance ratio (Eq. (8)):

$$a_{cdom}(350) = 0.5567^* \left(\frac{R_{rs}(443)}{R_{rs}(555)}\right)^{(-2.0421)} \quad (8)$$

The spectral slope S is estimated from $a_{cdom}(350)$ and $a_{cdom}(412)$ (Eq. (10)), this latter being also calculated from the blue to green reflectance ratio (Eq. (9)):

$$a_{cdom}(412) = X^* \left(\frac{R_{rs}(443)}{R_{rs}(555)}\right)^{(Y)} \quad (9)$$

$$S = 0.0058^* \left(\frac{a_{cdom}(412)}{a_{cdom}(350)}\right)^{(-0.9677)} \quad (10)$$

The parameter γ^0 in Eq. (7) takes into account the large variability of CDOM in coastal and ocean waters and is calculated as follows:

$$\gamma^0 = \frac{a_{cdom}(350) - \left(1/\gamma\right)}{a_{cdom}(350) + \left(1/\gamma\right)} \quad (11)$$

where γ is the slope of the hyperbolic model to estimate CDOM (Twardowski et al., 2004):

$$\gamma = 2.9332^* \left(\frac{a_{cdom}(412)}{a_{cdom}(350)}\right)^{(-0.7506)} \quad (12)$$

Shanmugam (2011) illustrated the good performance of their model through a validation exercise including 55 matchup data points based on NOMAD in situ and SeaWiFS estimated $a_{cdom}(443)$ covering a relatively narrow range of $a_{cdom}(443)$ values (from 0.01 to ~1 m^{-1}).

2.3.4. Loisel et al. (2014)

Loisel et al. (2014) developed a semi-analytical model for estimating $a_{cdom}(412)$ in coastal waters from ocean color remote sensing observations (CDOM-KD1). This model is based on the theoretical link between the vertical attenuation coefficient, $K_d(\lambda)$ and IOPs which has been reformulated as follows:

$$K_d(\lambda) = K_w(\lambda) + f(a_{cdom}(\lambda)) + \Delta_p(\lambda) \quad (13)$$

where K_w is the diffuse attenuation coefficient for pure sea water, $f(a_{cdom}(\lambda))$ is a function that depends exclusively on the absorption coefficient of CDOM and $\Delta_p(\lambda)$ is the contribution of particles in the attenuation process. To minimize the impact of scattering on the retrieval of a_{cdom} at 412 nm, the model involves the difference of $K_d(\lambda) - K_w(\lambda)$ at two specific wavelengths. Based on these different considerations the model formalism is expressed as follows:

$$a_{cdom}(412) = 10^{\left(0.15482^*(X)^2 + 1.1939^*(X) + 0.0689\right)} \quad (14)$$

where

$$X = \Delta K_d(412-560) - \Delta_p(412-560) \quad (15)$$

with

$$\Delta K_d(412\text{–}560) = \left(K_d(412) - K_w(412)\right) - \left(K_d(560) - K_w(560)\right) \quad (16)$$

and

$$\Delta_p(412-560) = 10^{\left(-0.009^*(log_{10}(\Delta K_d))^2 + 1.147^* log_{10}(\Delta K_d) - 0.26\right)} \quad (17)$$

In the context of remote sensing applications, ΔK_d is directly estimated from the R_{rs} using a parametrization developed from the IOCCG (2006) data set:

$$\Delta K_d(412-560) = 10^{\left(A^* log_{10}\left(\frac{Rrs(412)}{Rrs(560)}\right)^3 + B^* log_{10}\left(\frac{Rrs(412)}{Rrs(560)}\right)^2 + C^* log_{10}\left(\frac{Rrs(412)}{Rrs(560)}\right) + D\right)} \quad (18)$$

where A, B, C and D coefficients are −0.12484, 0.160857, −1.2292 and − 0.886471, respectively, for a sun angle (θ_s) of 30°.

Loisel et al. (2014) documented the overall good performance of their model over very contrasted coastal ecosystems. This has been illustrated from a validation exercise based on the NOMAD matchup data set which covers a large range of $a_{cdom}(412)$ values ($N = 109$, [0.02, 5.0 m^{-1}]) and includes uncertainties related to atmospheric corrections.

While this model has been developed for coastal water applications, the relationship between a_{cdom} and K_d on which it is based is still valid for open ocean waters.

3. Results and discussion

3.1. Adaptation of the Loisel et al. (2014) algorithm for estimating $a_{cdom}(443)$ over the global ocean

A new model, referred to as CDOM-KD2, which consists in an adaptation of the general semi- analytical coastal model published by Loisel et al. (2014), has been developed for estimating $a_{cdom}(443)$ over the global ocean. This adaptation was developed considering the synthetic DS1 data set.

3.1.1. CDOM-KD2 parameterization

Assuming a restricted CDOM absorption at 560 nm (see section 2.3.3) $a_{cdom}(443)$ can be expressed as follows:

$$\begin{matrix} a_{cdom}(443) \\ = f\left[\begin{matrix} (K_d(443) - K_w(443)) - (K_d(560) - K_w(560)) \\ -\Delta_p(443-560) \end{matrix} \right] \end{matrix} \quad (19)$$

The attenuation coefficient of light due to pure seawater, $K_w(\lambda)$, has been well documented (Morel and Maritorena, 2001; Morel et al., 2007). From literature K_w at 443 nm and 560 nm were set to 0.00948 and 0.0645 m^{-1} respectively (Morel et al., 2007; Loisel et al., 2014). Following the same approach of Loisel et al. (2014), $a_{cdom}(443)$ was empirically modeled as follows:

$$a_{cdom}(443) = 10^{[0.9902*X-0.0522]} \quad (20)$$

where

$$X = \Delta K_d(443–560) – \Delta_p(443–560) \quad (21)$$

with

$$\begin{matrix} \Delta K_d(443–560) \\ = (K_d(443) – K_w(443)) – (K_d(560) – K_w(560)) \end{matrix} \quad (22)$$

Δ_p (443–560), which considers the contribution of particulate matter to the attenuation of light, was parameterized from ΔK_d as follows:

$$\Delta_p(443-560) = 10^{[0.906*\log_{10}(\Delta K_d)-0.526]} \quad (23)$$

The model shows good accuracy over the whole range of $a_{cdom}(443)$ in DS1 (Fig. 3a; RMSD = 0.137m^{-1}, MAPD = 19.214% and MR = 1.059). The highest uncertainty is in the parameterization of X (RMSD = 0.11m^{-1}, MAPD = 15.06% and MR = −1.17).

3.1.2. Model development in the context of satellite application

In order to avoid the cumulative impact of the relative errors associated with the K_d estimation performed at each individual wavelength considered in CDOM-KD1, ΔK_d was assessed directly from $R_{rs}(\lambda)$ using empirical formulations based on Hydrolight simulations (Loisel et al., 2014). In the present study, the calculation of ΔK_d is now performed through a Neural Network (NN) approach, following the same training data set and protocol of the NN originally developed in Jamet et al. (2012) for estimating $K_d(\lambda)$ in the visible domain.

This NN consists in a Multi-Layer Perceptron model (MLP, Rumelhart et al., 1986) based on 7 possible input parameters including the R_{rs} at 412, 443, 490, 510, 560 and 670 nm and the sun angle, θ_s. In practice, $R_{rs}(412)$ was not used in the model definition due to the general high uncertainty level associated with the satellite R_{rs} signal at this spectral band in coastal waters (Goyens et al., 2013; Jamet et al., 2012; Mélin et al., 2007; Pahlevan et al., 2021; Zibordi et al., 2006). The reflectance in the red part of the spectrum ($R_{rs}(670)$) was considered as an input of the model depending on the relative level of turbidity of the water. This selective definition was performed considering the impact of the low signal to noise ratio on the satellite R_{rs} data validity in the red spectral domain, this issue being particularly relevant when dealing with non-turbid water environments (e.g., Hu et al., 2012). Following the recent works by Loisel et al. (2018), a switch criterion was therefore used to differentiate non-turbid and turbid waters. In practice, data showing a $R_{rs}(490)/ R_{rs}(560)$ ratio lower or equal to 0.85, were considered as turbid. In this case the R_{rs} input for the NN were restricted to the range 443–670 nm, while the model considered has two hidden layers with five neurons for each layer. On the other hand, if the previous ratio was higher than 0.85, emphasizing the presence of non-turbid water, the input R_{rs} values were ranging from 443 to 560 nm and the NN has two hidden layers with four neurons for each layer.

The impact of this Neural Network algorithm for estimating ΔK_d on the overall performance of the $a_{cdom}(443)$ inversion model (CDOM-KD2) has been evaluated on the synthetic dataset considering a sun zenith angle of 30° (Fig. 3). The results indicate a similar $a_{cdom}(443)$ retrieval accuracy when ΔK_d is directly obtained from the $K_d(\lambda)$ of the synthetic data set (DS1, e.g. MAPD = 19%, Fig. 3 a) or from the ΔK_d computed from the $R_{rs}(\lambda)$ using the NN model (e.g. MAPD = 23%, Fig. 3 b).

3.2. Intercomparison and validation of $a_{cdom}(443)$ inversion models

3.2.1. Performance and inter-comparison of the different $a_{cdom}(443)$ inversion models with the in situ and matchup data sets

The performance of the A2018, C2017, S2011 and CDOM-KD2 models have been first evaluated for global scale application (including coastal and open ocean waters) from the DS2 in situ validation data set (Fig. 4 a, e, i, m). The models C2017, S2011 and CDOM-KD2, which are based on distinct formalisms and assumptions, show an overall general satisfying accuracy in the retrieved $a_{cdom}(443)$ over the 3 orders of magnitude covered in DS2 (e.g. MAPD of 49.22, 39.57

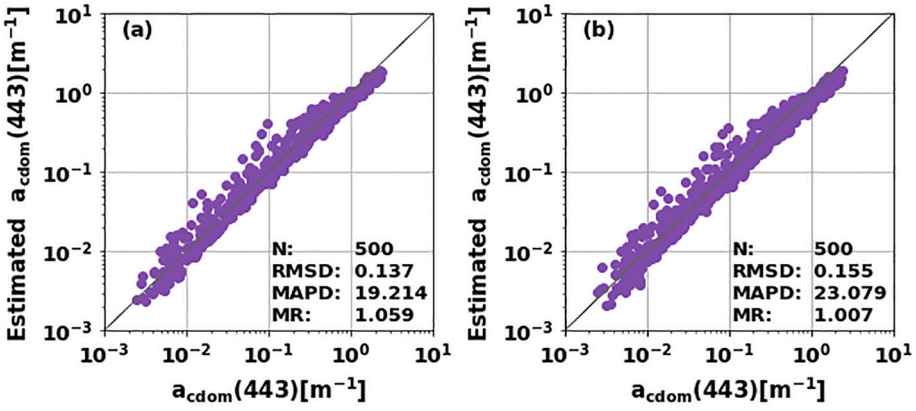

Fig. 3. Performance of the CDOM-KD2 inversion model over the DS1 data set considering ΔK_d calculated with the measured K_d (a) or with the NN based inversion model (Eq. (20)) (b).

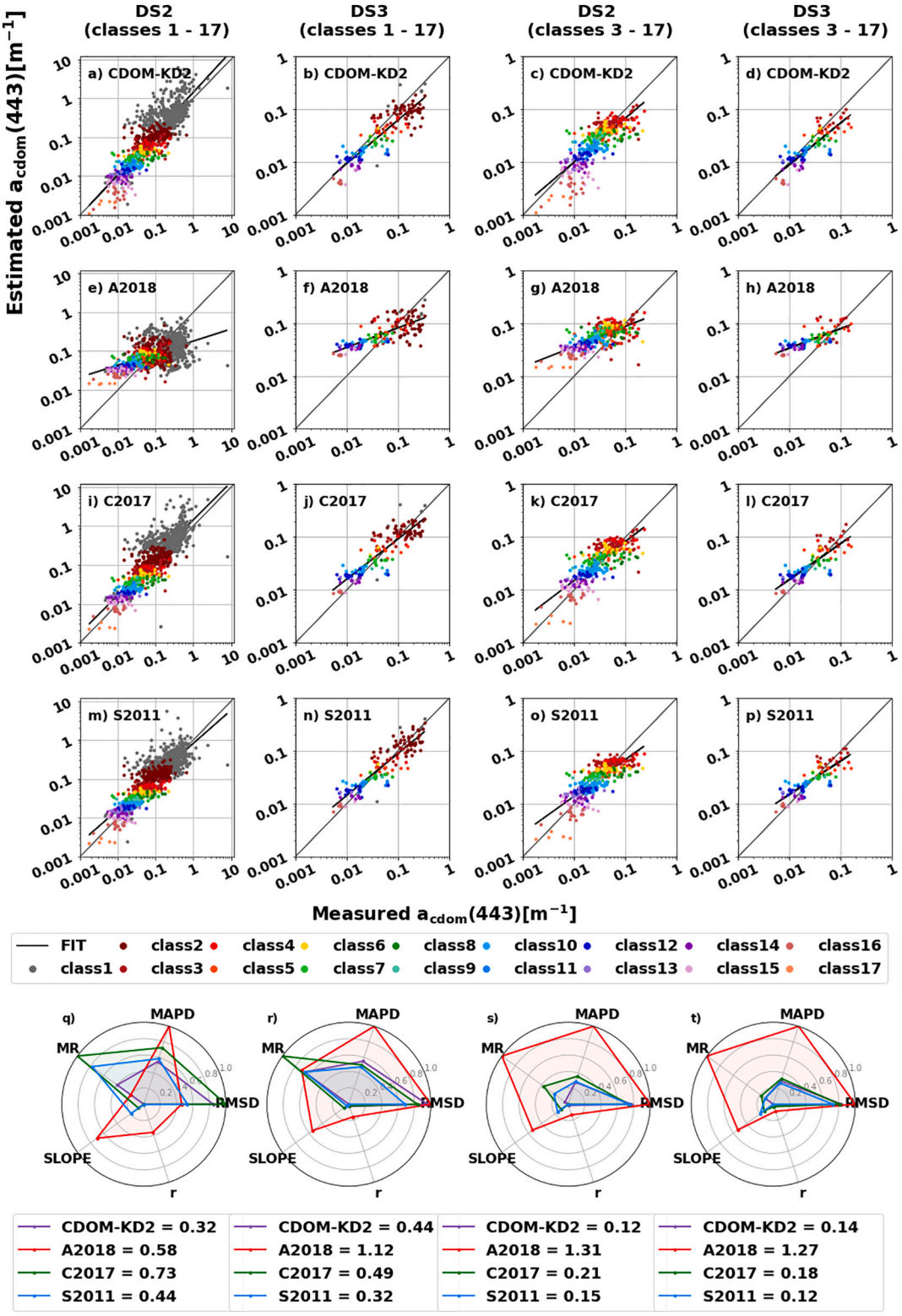

Fig. 4. Validation scatterplots of the four tested models (CDOM-KD2, A2018, C2017 and S2011) using the complete data sets (classes 1 to 17) of DS2 (a, e, i, m) and DS3 (b, f, j, n) and their respective radar plots summarizing the statistics used for evaluating the four models (q, r). The same information is provided for the non-turbid subsets (classes 3 to 17) of DS2 (c, g, k, o) and DS3 (d, h, l, p) and their respective radar plots (s, t).

and 36.95%, respectively). This general feature is also underlined by the overall similarities in the range and statistics reported in Table 1 for the latter three models. On the other hand, the global performance of A2018 for estimating $a_{cdom}(443)$ significantly departs from the others. The range of $a_{cdom}(443)$ values retrieved by Aurin et al. (2018) model is considerably narrower than that for the other three models (Table 1) as a consequence of the large overestimation of A2018 derived $a_{cdom}(443)$ values for low and moderate a_{cdom} loads ($a_{cdom}(443) < 0.1\ m^{-1}$, Fig. 4 e). As well as to the sharp underestimation of the highest A2018-derived $a_{cdom}(443)$ values ($a_{cdom}(443) > 0.1\ m^{-1}$, Fig. 4 e). This confirms the

Table. 1
Summary table of the performance of $a_{cdom}(443)$ inversion models (CDOM-KD2, A2018, C2017, S2011) on the different evaluation data sets (DS2 and DS3) considered as a whole (classes 1–17) or focusing on non-turbid waters (classes 3–17). For each in situ validation subset descriptive statistics are provided (N: number of data points, $\overline{X}$: mean values, m: median value, std.: standard deviation value). The former statistics are also provided for the $a_{cdom}(443)$ data estimated from each inversion model together with additional model performance statistical descriptors (RMSD (m^{-1}), MAPD (%), MR).

	N	RANGE [m^{-1}]	$\overline{X}$ [m^{-1}]	m [m^{-1}]	std [m^{-1}]	Slope	r	RMSD [m^{-1}]	MAPD [%]	MR
Classes 1–17										
DS2	**1001**	**[0.002–7.84]**	**0.18**	**0.09**	**0.31**					
CDOM-KD2		[0.001–6.15]	0.32	0.12	0.62	1.05	0.86	0.58	36.95	1.26
A2018		[0.014–0.73]	0.11	0.1	0.1	0.31	0.55	0.31	67.78	0.87
C2017		[0.002–14.2]	0.34	0.15	0.7	0.97	0.86	0.68	49.22	1.65
S2011		[0.002–5.6]	0.2	0.14	0.3	0.85	0.86	0.36	39.57	1.51
DS3	**166**	**[0.005–0.33]**	**0.08**	**0.04**	**0.08**					
CDOM-KD2		[0.004–0.31]	0.05	0.04	0.05	0.82	0.88	0.06	36.79	0.82
A2018		[0.025–0.28]	0.07	0.05	0.04	0.37	0.76	0.06	66.67	1.2
C2017		[0.009–0.41]	0.08	0.06	0.07	0.76	0.89	0.05	33.62	1.27
S2011		[0.007–0.4]	0.08	0.05	0.08	0.8	0.91	0.04	31.87	1.03
Classes 3–17										
DS2	**372**	**[0.002–0.23]**	**0.04**	**0.03**	**0.04**					
CDOM-KD2		[0.001–0.12]	0.03	0.03	0.02	0.83	0.79	0.03	27.42	1.04
A2018		[0.014–0.16]	0.06	0.06	0.03	0.38	0.69	0.04	97	1.87
C2017		[0.002–0.14]	0.04	0.04	0.03	0.74	0.8	0.03	34.77	1.32
S2011		[0.002–0.09]	0.04	0.04	0.02	0.69	0.8	0.03	28.11	1.19
DS3	**108**	**[0.005–0.15]**	**0.06**	**0.02**	**0.03**					
CDOM-KD2		[0.004–0.1]	0.03	0.02	0.02	0.79	0.84	0.02	30.85	0.85
A2018		[0.025–0.13]	0.05	0.05	0.03	0.37	0.77	0.03	103.18	2.18
C2017		[0.01–0.17]	0.04	0.03	0.03	0.68	0.82	0.02	33.92	1.21
S2011		[0.007–0.11]	0.03	0.03	0.02	0.63	0.85	0.02	27.98	1.21

results by Aurin et al. (2018) who emphasized the lower performance of this empirical model for estimating a_{cdom} at wavelengths >412 nm especially when using SeaWIFS bands as input values.

The use of the optical typology provided by Mélin and Vantrepotte (2015) provides a finer characterization of the model performances. The class-based distribution further confirms the global relevance of C2017, S2011 and CDOM-KD2 derived $a_{cdom}(443)$ values with a general satisfying accuracy over the 17 waters types considered. A lower precision in the retrieved $a_{cdom}(443)$ is however observed for the three latter models in the most turbid waters (Class 1) as underlined by the higher scatter in the Fig. 4 a, e and m for the corresponding samples. Further, a slight overestimation of the highest $a_{cdom}(443)$ values is found for the $a_{cdom}(443)$ values derived from CDOM-KD2 and C2018 for the samples associated with the Class 1. The difficulty to estimate CDOM in such highly turbid environments from general formulations requires the development of specific inversion models. While few formulations have been proposed for estimating $a_{cdom}(\lambda)$ in optically complex waters (e.g. Loisel et al., 2014; Cao et al., 2018) CDOM estimates in coastal environments are often derived from regional models (Cao et al., 2018; Mannino et al., 2014; Matsuoka et al., 2013).

The radar plot for the whole data set DS2 (Fig. 4 q), which provides a synthetic view of the accuracy of the different models considered for estimating $a_{cdom}(443)$, confirms the previous results further underlining the vicinity in the performance of the C2017, S2011 and CDOM-KD2 with a slightly better general performance for the CDOM-KD2 method.

Results obtained considering the whole DS3 matchup data set are globally in line with those derived from the DS2 validation data with a general satisfying and comparable accuracy for C2017, S2011 and CDOM-KD2 (MAPD of 33.62, 31.87 and 36.79%, Fig. 4 b, j, n) and lower general performance of the A2018 model (MAPD 66.67%, Fig. 4 f). The differences in the coverage provided by DS2 and DS3 induced slight modulations in the finer patterns. An underestimation of the highest $a_{cdom}(443)$ values in DS3 is for instance observed for the CDOM-KD2 model while the reverse situation was found for DS2 which accounts for a higher amount of CDOM rich waters (> 0.5 m^{-1}).

3.2.2. *Comparison of the $a_{cdom}(443)$ models on moderate to non-turbid waters*

The performance of the different $a_{cdom}(443)$ inverse methods was further evaluated for open waters applications focusing only on the moderate to non-turbid data. For that purpose, the validation exercise is now performed excluding from DS2 and DS3 the ultra-turbid samples corresponding to the Mélin and Vantrepotte (2015) Class 1 and Class 2 waters. The new DS2 and DS3 data sets are now composed by 373 (instead of 1001) and 108 (instead of 166) data points, respectively. The main features described previously on the whole data sets are globally observed from these restricted datasets with an overall satisfying performance of the inversion of $a_{cdom}(443)$ values in oceanic waters. For instance, the MAPD (and slope) values for C2017, S2011 and CDOM-KD2 are 34.77% (0.74), 28.11% (0.69) and 27.42% (0.83) for DS2 and 33.92% (0.68), 27.98% (0.63) and 30.85% (0.79) for DS3, respectively). As with previous results obtained on the whole data sets the performances of these three models overcome that of the A2018 (Fig. 4 g, h) inversion algorithm (MAPD of 97% and 103.18% and slope of 0.38 and 0.37 for DS2 and DS3, respectively).

The comparison of the overall statistics for the C2017, S2011 and CDOM-KD2 models further confirms the general consistency in the $a_{cdom}(443)$ retrieval from these three different approaches, which precision is generally increased when excluding the most turbid environments. Among the three latter formulations, the CDOM-KD2 model shows slightly better overall performance considering both in situ (Fig. 4 s) and matchup (Fig. 4 t) data sets. The CDOM-KD2 model slightly underestimates $a_{cdom}(443)$ in ultra-oligotrophic waters (classes 16 and 17). This feature needs however to be confirmed from a larger validation dataset considering the relatively low number of data points depicting these water types (classes 16 and 17) in DS2 ($N = 20$) and DS3 ($N = 6$).

It is worth noting that the S2011 model strongly depends on the blue to green reflectance ratio which is also used for estimating *Chl-a* concentration in offshore waters. Knowing that in the open ocean these two components may temporally be lagged by 2 to 5 weeks (Hu et al., 2006; Organelli et al., 2014), the use of common inputs for assessing both

CDOM and *Chl-a* might tend to artificially strengthen the co-variation between these two variables (Supplementary Fig. 1). Moreover, the $a_{cdom}(443)/a_{cdm}(443)$ ratio values estimated at global scale using S2011 (for $a_{cdom}(443)$) and GSM (for $a_{cdm}(443)$) present numerous unrealistic values, the mean and standard variation values being of 1.0 ± 0.63 over the 10-years GlobColour climatology (Supplementary Fig. 1 b). The CDOM-KD2 model was therefore selected for describing the global scale spatio-temporal variability of $a_{cdom}(443)$ and of the relative contribution of CDOM to the absorption of the whole detrital matter pool as depicted by the ratio $a_{cdom}(443)/a_{cdm}(443)$.

3.2.3. Global $a_{cdom}(443)$ and $a_{cdom}(443)/a_{cdm}(443)$ spatio-temporal patterns

The global scale spatial distribution variation coefficient of CDOM-KD2 derived $a_{cdom}(443)$ is depicted in Fig. 5 a and c from the GlobColour L3 10-year archive average map (April 2002–April 2012). The CDOM-KD2 outputs together with the $a_{cdm}(443)$ derived from the GSM model were used to compute $a_{cdom}(443)/a_{cdm}(443)$ (Fig. 5 b and d) and further depict the spatio-temporal variability of the relative importance of the dissolved matter into the total detrital matter absorption.

$a_{cdom}(443)$ shows a high spatial dynamic with values ranging over 3 orders of magnitude ($a_{cdom}(443) < 0.001$ m^{-1} to >2 m^{-1}). The global spatial distribution patterns of $a_{cdom}(443)$-CDOM-KD2 generally agrees with the distribution patterns expected and previously described by other authors. High CDOM values are found in coastal waters and in the sub-polar and equatorial areas, while low values are located throughout the subtropics (Siegel et al., 2005a; Nelson and Siegel, 2013). Lowest values are found in the oligotrophic gyre areas such as the South Pacific Gyre, where estimated values are in agreement with in situ observations performed in the area (Bricaud et al., 2010, minimum $a_{cdom}(440) \approx 0.001$ m^{-1}). In line with Bricaud et al. (2012), $a_{cdom}(443)$ values at latitudes higher than 30° are generally higher in the northern hemisphere and relatively lower in the southern hemisphere.

The CDOM-KD2 algorithm was also applied to OLCI L3 4-year data at global scale. OLCI $a_{cdom}(443)$ (Supplementary Fig. 2) globally shows similar spatial patterns with GlobColour data although OLCI $a_{cdom}(443)$ reaches more extreme end-member values than the GlobColour 10-year average merged data (lower values in the ultra-oligotrophic and higher ones in eutrophic waters, respectively).

Several works have considered the $a_{cdom}(443)/a_{cdm}(443)$ ratio as spatially and temporally quasi invariant or constant assuming CDOM to be the major contributor (> 80%) to CDM in the blue spectral domain (Nelson et al., 1998; Swan et al., 2009). However, the GlobColour 10-year average map shows that the ratio $a_{cdom}(443)/a_{cdm}(443)$ is highly variable in space, ranging from about 0.2 to almost 1 (Fig. 5 b), with spatial distribution patterns similar to those depicted for $a_{cdom}(443)$ (Fig. 5). The overall global average value of $a_{cdom}(443)/a_{cdm}(443)$ for the GlobColour 10-year archive reaches 0.61 ± 0.14 being significantly lower than the values reported previously (Nelson et al., 1998, Swan et al., 2009). The lowest ratio values (0.2 to 0.5) are located in the oligotrophic gyre waters. Besides the expected presence of high $a_{cdom}(443)/a_{cdm}(443)$ values over some coastal environments (e.g. Baltic and Black seas), the relative contribution of CDOM to CDM generally tends to increase in oceanic waters from mid to high latitudes (> 30°) reaching maximum values (around 0.9) in polar regions. High $a_{cdom}(443)/a_{cdm}(443)$ values are also found in the equatorial Pacific

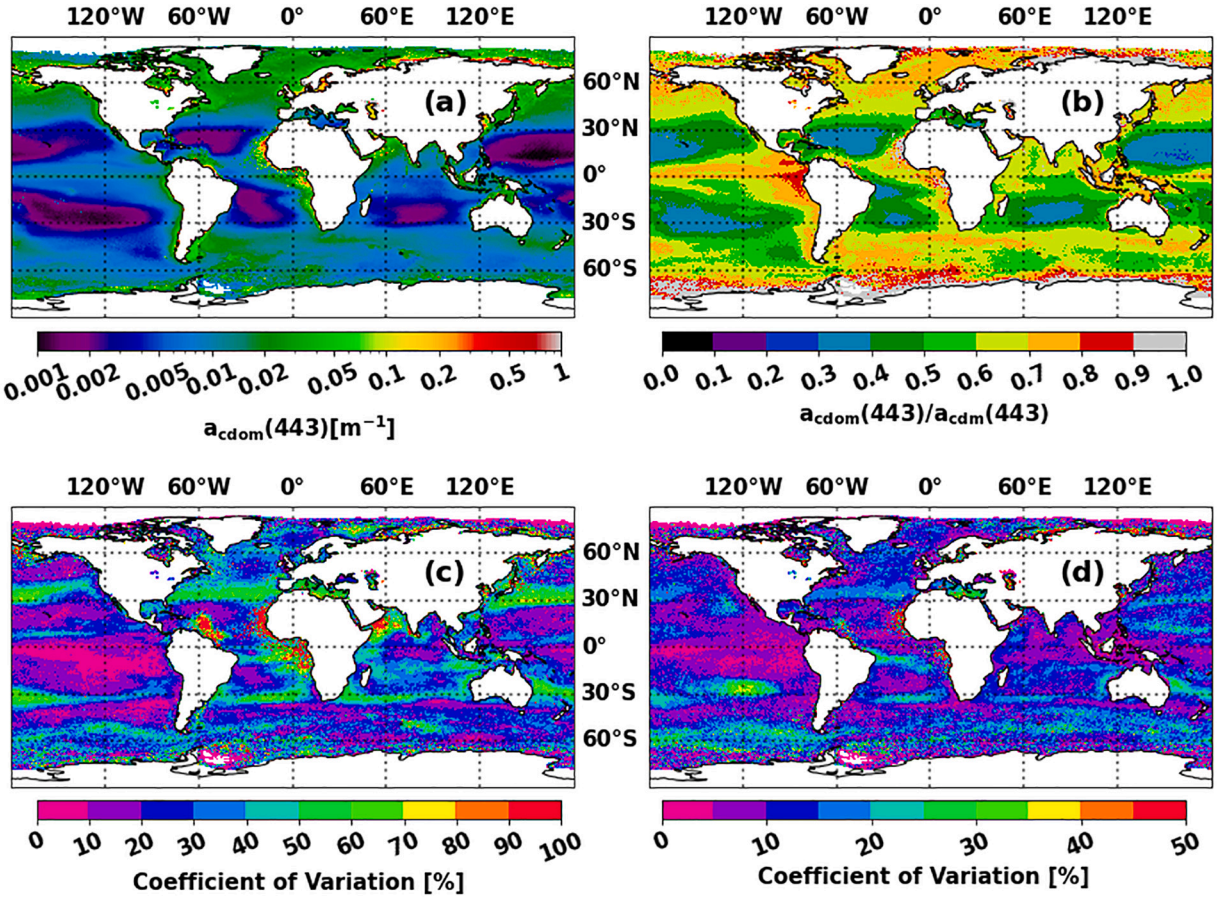

Fig. 5. (a) Global average $a_{cdom}(443)$ [m^{-1}] map produced with GlobColour L3 merged 25 km 8 days composite data from 23rd April 2002 to 13th April 2012 and CDOM-KD2 model and (c) its coefficient of variation. (b) Annual average $a_{cdom\text{-}KD2}(443)/a_{cdm}(443)$, with $a_{cdm}(443)$ derived from the GSM model over the same time period and (d) its coefficient of variation [%].

(>0.7) and Atlantic (>0.6) waters.

The coefficient of variation (CV = standard deviation / mean * 100, in %) maps computed from the GlobColour L3 merged 8-day composite archives of $a_{cdom}(443)$ (Fig. 5 c) and of $a_{cdom}(443)/a_{cdm}(443)$ (Fig. 5 d) also show similar spatial distribution patterns. An overall larger temporal variability is however found for $a_{cdom}(443)$ than for $a_{cdom}(443)/a_{cdm}(443)$ (global average CV of 32 ± 18% and 14 ± 11%, respectively). This discrepancy in terms of temporal variability level is particularly marked in open ocean waters where $a_{cdom}(443)$ CV values range between 10 and 70% while it varies between 2 and 35% for $a_{cdom}(443)/a_{cdm}(443)$.

Globally, the highest temporal dynamics for both $a_{cdom}(443)$ and $a_{cdom}(443)/a_{cdm}(443)$ (CV > 80% and > 50%, respectively) are mostly found in areas influenced by terrestrial inputs of CDOM. Such high temporal variations are found for instance within the oceanic water influenced by the Amazon - Orinoco systems where the observed strong modulation in the surface CDOM loads are related to the combined effect of the highly variable regional currents system and the seasonal dynamics of the terrestrial inputs associated with these two large river systems (Salisbury et al., 2011; López et al., 2012). The high $a_{cdom}(443)$ temporal variability found in the western Africa and Arabian sea waters can be more likely related to the influence of desert dusts on the temporal coverage and radiometric quality of the OCR observations.

In open ocean waters, not affected by terrestrial influence, the highest temporal dynamics of $a_{cdom}(443)$ (CV > 60%) and $a_{cdom}(443)/a_{cdm}(443)$ (CV > 15%) are found in areas strongly influenced by main oceanic currents and upwelling areas. The impact of the oceanic circulation is particularly visible within water masses surrounding oceanic gyres as well as within three latitudinal bands located around 10°N, 30° N and 30° S where $a_{cdom}(443)$ CV ranges from 40% to 70% and $a_{cdom}(443)/ a_{cdm}(443)$ CV ranges from 10% to 35% over the 10-year GlobColour time period. Strong temporal dynamics are also clearly visible along the Antarctic Polar Frontal Zone (APFZ; $a_{cdom}(443)$ CV = [50% - 70%] and $a_{cdm}(443)$ CV = [10% - 40%]) characterized by the presence of a marked seasonality in the water mass characteristics due to the occurrence of a strong phytoplankton spring bloom (Abbott et al., 2000; Tremblay et al., 2002). Similar relatively high CV values are found in the Mediterranean Sea for $a_{cdm}(443)$ and eastern Mediterranean Sea for $a_{cdom}(443)/a_{cdm}(443)$, reflecting the original character of these areas in terms of optical properties (Claustre et al., 2002; Loisel et al., 2011; Morel and Gentili, 2009).

On the other hand, very stable areas for $a_{cdom}(443)$ and $a_{cdom}(443)/a_{cdm}(443)$ (CV < 10%) are detected mainly in the oceanic gyres, in the waters located between [40°-60°] North and South latitudinal layers and in the northern Indian ocean. The latter areas coincide with the most oligotrophic regions of the ocean (gyres) as well as with oceanic regions located between the main oceanic currents. An exception to the latter general pattern is however noticed for $a_{cdom}(443)/a_{cdm}(443)$ in the SPG which shows particularly high temporal dynamics with CV > 25% in the most oligotrophic waters.

While explaining the apparent decoupling between a_{cdom} and a_{nap} at global scale is beyond the scope of the present work, our results do not support the widespread assumption of an overall global dominant and temporally slightly variable contribution of CDOM to CDM. This pattern further emphasizes the need to deeply investigate the dynamics and environmental factors controlling the dissolved and particulate components of the ocean detrital matter pool.

For completeness, the global scale contribution of $a_{cdom}(443)$ to $a_{nw}(443)$ was also calculated considering the 10 year GlobColour data set (Supplementary Fig. 3). The ratio of $a_{cdom}(443)/a_{nw}(443)$ (mean = 0.42 ± 0.29, range = [0.1–0.9]) shows similar distribution patterns to those reported previously for $a_{cdom}(443)/a_{cdm}(443)$. The temporal dynamics for that ratio depicted from the corresponding CV values also shows spatial patterns very close to that already depicted for $a_{cdom}(443)/a_{cdm}(443)$ although presenting relatively more extreme values probably linked to the additional consideration phytoplankton activity, and less variability in the APFZ.

3.2.4. Global scale covariation between a_{cdom}, a_{cdm} and Chl-a dynamics

Over oceanic waters the temporal dynamics of CDM is assumed to be primarily driven by phytoplankton and associated by products variability (Siegel et al., 2005b; Bricaud et al., 2012). In the open ocean, CDOM is the dominant component of CDM (Siegel et al., 2002; Kopelevich and Burenkov, 1977). Therefore, CDOM is expected to be highly related to CDM and Chl-a dynamics, although a robust statistical relationship between the latter variables has not been found at an oceanic basin-scale (Siegel et al., 2002). The covariation between CDOM (CDOM-KD2 derived), CDM and *Chl-a* (GSM estimates) was specifically examined through correlation maps based on the 10-year Globcolour 8 days composite archive (Fig. 6).

A general very high positive correlation between CDOM and CDM prevails over a large part of the global ocean ($r > 0.9$). However, lower values ($r < 0.6$) are observed over all oceanic gyre regions where the correlation between $a_{cdom}(443)$ and $a_{cdm}(443)$ decrease towards the gyre center (Fig. 6 a), where $a_{cdom}(443)/a_{cdm}(443)$ ratio shows its minimal values (Fig. 5 b), reaching values close to zero in the North and South Pacific gyres. Relatively low CDOM to CDM correlation levels (r = [0.5–0.6]) are also observed in the Pacific sub-Arctic and sub-Antarctic gyre waters, Pacific equatorial divergence area and patchy regions of the Antarctic waters.

Globally, oceanic areas where CDOM and CDM exhibit lower correlation, show contrasted patterns regarding their correlation with *Chl-a* (Fig. 6 b and c). This is particularly marked over the gyres, where CDOM-*Chl-a* correlation levels are generally lower than those observed for CDM-*Chl-a*. This feature can be related to the low contribution of CDOM to CDM (Fig. 5 b) in these very oligotrophic areas as well as to the processes regulating the CDOM and CDM dynamics. In the open ocean,

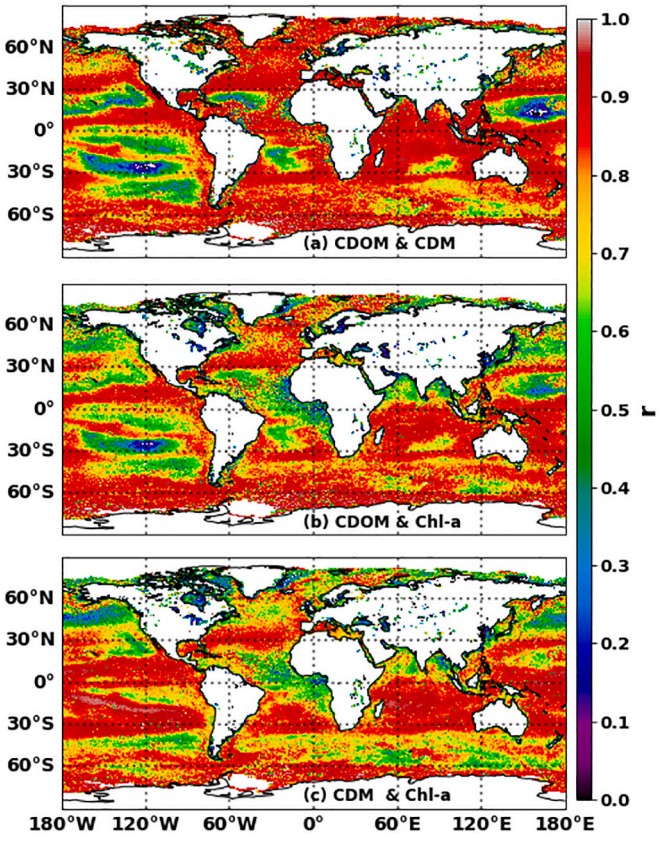

Fig. 6. Correlation maps between (a) CDOM-KD2 and a_{cdm}, (b) CDOM-KD2 and Chl-a, (c) a_{cdm} and Chl-a. White areas represent pixels where either there is no data available or where the correlation is not significant ($p > 0.05$).

CDOM is mainly produced by phytoplankton and associated by-products. Meanwhile, CDOM degradation is driven by photochemical processes (Chen and Bada, 1992; Siegel et al., 2005b) and microbial activity (Fichot and Benner, 2012; Nelson et al., 2004). In oligotrophic regions, such as the Sargasso Sea or the Mediterranean Sea, where a relative low correlation was found between CDOM and Chla, the production of CDOM is mainly driven by bacterial activity, the CDOM peak happens 2 to 5 weeks after the Chl-a maximum and coincides with bacteria maximal concentration (Hu et al., 2006; Organelli et al., 2014). In ultra-oligotrophic waters like the gyres the high bacterial activity due to the presence of an efficient microbial loop (Raimbault et al., 2008), also act as a significant source of CDOM. The double role of the bacterial community (source and sink of CDOM) in the nutrient depleted areas of the ocean generates great fluctuations on CDOM concentration in periods of days (Nelson et al., 2004) and might explain, together with photodegradation rates (Stedmon and Nelson, 2014), the observed low CDOM-Chl-a correlation for these regions. On the other hand, in ultra-oligotrophic waters the particulate fraction of CDM is strongly regulated by phytoplankton activity (Bricaud et al., 2010) what is reflected in great correlation between CDM-*Chl-a*.

These latter features are illustrated from time series extractions of $a_{cdom}(443)$, $a_{cdm}(443)$, and *Chl-a* over two contrasted oceanic areas, the South Pacific Gyre (SPG) and the North Atlantic (NA) (Fig. 7). In the very clear waters of the South Pacific Gyre (Fig. 7 b) the CDOM time series exhibits higher level of noise without real seasonal pattern while CDM and *Chl-a* follow the same annual cycle. The latter result is in line with in situ observations by Bricaud et al. (2010) along the BIOSOPE transect. They reported that small-scale changes in the phytoplankton biomass in the most oligotrophic waters of the SPG (*Chl-a* < 0.1 mg m^{-3}) do not induce significant variation in the CDOM content (their Fig. 14), in contrast to the non-algal particles (a_{nap}) which shows a high correlation with *Chl-a* (their Fig. 10). In contrast, a strong co-variation between Chl-a, $a_{cdom}(443)$, and $a_{cdm}(443)$ characterizes the times series extracted from the NA station (Fig. 7c), with the clear presence of a spring maximum for all of the parameters. At this area, CDOM is mainly locally produced by phytoplankton excretions and lysis (Nelson and Siegel, 2002). Therefore, the phytoplankton bloom is the main driver of both the particulate and dissolved detrital matter dynamics (Dutkiewicz et al., 2001; Lévy et al., 2005) showing no apparent lag in the $a_{cdom}(\lambda)$ and $a_{cdm}(\lambda)$ dynamics (on 8 days composite data).

4. Conclusions

A new model for assessing the $a_{cdom}(443)$ global distribution from OCR (CDOM-KD2) has been developed adapting an existing semi-analytical formalism (Loisel et al., 2014) based on the use of the vertical attenuation coefficient of the downwelling irradiance, K_d. Among the four models evaluated: Aurin et al. (2018), Shanmugam (2011), Chen et al. (2017) and CDOM-KD2, the last three methods, although based on different assumptions, show consistent performances at estimating surface $a_{cdom}(443)$ values at global scale. The CDOM-KD2 inversion model performs slightly better when considering both the in situ (DS2) and matchup (DS3) data sets used in the frame of this study, especially over open ocean waters. These results clearly underline the actual possibility to specifically estimate $a_{cdom}(443)$ at global scale and to overcome limitations related to the use of $a_{cdm}(443)$ especially for open ocean dedicated studies related to the DOC dynamics analysis.

The CDOM-KD2 model was applied to global satellite archives of merged (GlobColour) or individual recent satellite (OLCI) to characterize the $a_{cdom}(443)$ spatio-temporal patterns of variability as well as that of the contribution of CDOM to CDM and of CDOM to the non-water absorption. While the $a_{cdom}(443)$ as well as CDOM relative contribution

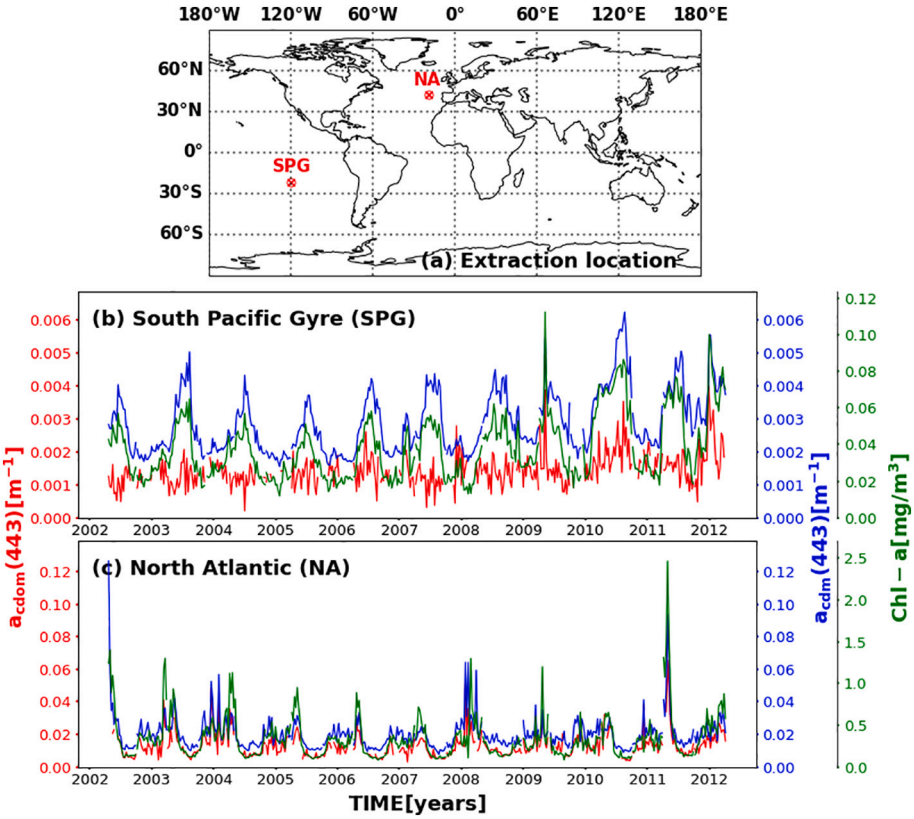

Fig. 7. (a) Location of the stations considered for the two time series plotted in panels (b) and (c) (red circles). At these two stations the correlation between a_{cdom} and both Chl-a and a_{cdm} is minimum (South Pacific Gyre: SPG) and maximum (North Atlantic, NA). Time series of $a_{cdom}(443)$, $a_{cdm}(443)$ and Chl-a at SPG (b) and NA (c). (For interpretation of the references to color in this figure legend, the reader is referred to the web version of this article.)

in both CDM and total absorption spatial variability are particularly marked between terrestrial influenced water masses and oceanic gyres end-members, a relative restricted temporal variability (10 year CV <50%) is in contrast generally observed in most of the oceanic domains.

Globally, in oceanic gyres, where CDOM loads are the lowest ($a_{cdom}(443)$ <0.002 m^{-1}), CDOM is not dominant in the total detrital matter absorption budget (<40%) representing also a reduced fraction of the total water absorption (<30%), these general features being slightly variable in time (CV < 10%). In these oceanic regions, correlation analysis reveals that CDOM dynamics is generally slightly coupled with that of CDM and Chl-*a* which both conversely show a strong co-variation. This tends to indicate that phytoplankton dynamics is the main driver of the particulate detrital matter variability in gyre systems whereas dissolved organic matter dynamics cannot be considered as a direct function of phytoplankton and phytoplankton by-products. This further underlines that other forcing parameters such as microbial and light dependent processes act as the main controlling factors explaining CDOM dynamics in these gyre systems. An exception to the previous general patterns is however observed in the most oligotrophic waters of the eastern SPG where a highest temporal variability (CV > 35%) is found for the $a_{cdom}(443)/a_{cdm}(443)$ and $a_{cdom}(443)/a_{nw}(443)$ ratios when compared to the other gyre waters. Further, the contribution of CDOM to the total absorption in the latter area is also higher than that for the other gyre waters (>40%) suggesting the presence of a higher decoupling between particulate and dissolved matter dynamics for that region.

In contrast with gyres areas, polar and oceanic waters influenced by large river inputs globally show the highest values and a high temporal variability for $a_{cdom}(443)$, $a_{cdom}(443)/a_{cdm}(443)$ and $a_{cdom}(443)/a_{nw}(443)$ ratios. In the corresponding regions CDOM represents 60% or more of CDM while a general high coupling in the dynamics of the dissolved and particulate detrital matter prevails. The latter components do not necessarily covary with phytoplankton dynamics especially in areas significantly impacted by terrestrial inputs. Subtropical (around 30°N and S) and Equatorial regions show and intermediate situation with an overall moderate level of temporal variability for $a_{cdom}(443)$, $a_{cdom}(443)/ a_{cdm}(443)$ and $a_{cdom}(443)/a_{nw}(443)$ ratios.

This apparent heterogeneity in the CDOM, CDM and Chl-a dynamics, and thus in the factors controlling both dissolved and particulate matter variability in the global ocean should be further investigated. Further, the high variability observed in the relative contribution of CDOM to the total absorption might be considered in future works for more precisely quantifying the impact of CDOM on *Chl-a* estimates over oceanic waters from OCR.

Declaration of Competing Interest

The authors declare that they have no known competing financial interests or personal relationships that could have appeared to influence the work reported in this paper.

Acknowledgments

The study was funded by the European Commission's Copernicus Program and EUMETSAT, contract number EUM/CO/17/4600001980/EJK as well as by the French Spatial Agency (CNES) through the TOSCA program in the frame of the DOC project (PI. H. Loisel). The PhD funding of Ana Gabriela Bonelli was covered by CNES and ACRI-ST. The authors acknowledge the two anonymous reviewers and Aurea Maria Ciotti for their valuable suggestions which have helped to improve the quality of the manuscript. The authors also acknowledge NASA, and especially Antonio Mannino, for providing access to GOCAD dataset. The authors would like to thank all participants and voluntary contributors for collecting data that have been assembled in the NOMAD data set. We would also like to recognize the time and effort done to collect the in situ measurements gathered in this study, which were collected by different research groups and for different areas across the globe. We also thank ESA, EUMETSAT and ACRI-ST for freely processing and providing Sentinel-3 images.

Appendix A. Supplementary data

Supplementary data to this article can be found online at https://doi.org/10.1016/j.rse.2021.112637.

References

Abbott, M.R., Richman, J.G., Letelier, R.M., Bartlett, J.S., 2000. The spring bloom in the Antarctic polar frontal zone as observed from a mesoscale array of bio-optical sensors. Deep Sea Res., Pt. II 47, 3285–3314. https://doi.org/10.1016/S0967-0645(00)00069-2.

Aurin, D., Mannino, A., Lary, D., 2018. Remote sensing of CDOM, CDOM spectral slope, and dissolved organic carbon in the Global Ocean. Appl. Sci. 8, 2687. https://doi.org/10.3390/app8122687.

Bailey, S., Wang, M., 2001. Satellite aerosol optical thickness match-up procedures. In: NASA Tech. Memo., 2001-209982. NASA Goddard Space Flight Center, Greenbelt, MD, pp. 70–72.

Blough N.V., and Del Vecchio, R., 2002. Chromophoric DOM in the coastal environment, Biogeochemistry of Marine Dissolved Organic Matter, D. A. Hansell, C. A. Carslon, Academic.

Boss, E., Roesler, C., 2006. Over constrained linear matrix inversion with statistical selection. In: Lee, Z.P. (Ed.), IOCCG Reports, 5. IOCCG, Dartmouth.

Bricaud, A., Morel, A., Prieur, L., 1981. Absorption by dissolved organic matter of the sea (yellow substance) in the UV and visible domains. Limnol. Oceanogr. 26, 43–53. https://doi.org/10.4319/lo.1981.26.1.0043.

Bricaud, A., Babin, M., Claustre, H., Ras, J., Tieche, F., 2010. Light absorption properties and absorption budget of Southeast Pacific waters. J. Geophys. Res. Oceans 115. https://doi.org/10.1029/2009JC005517.

Bricaud, A., Ciotti, A.M., Gentili, B., 2012. Spatial-temporal variations in phytoplankton size and colored detrital matter absorption at global and regional scales, as derived from twelve years of SeaWiFS data (1998–2009). Global Biogeochem. Cy. 26, GB1010 https://doi.org/10.1029/2010GB003952.

Cao, F., Tzortziou, M., Hu, C., Mannino, A., Fichot, C.G., Del Vecchio, R., Najjar, R.G., Novak, M., 2018. Remote sensing retrievals of colored dissolved organic matter and dissolved organic carbon dynamics in North American estuaries and their margins. Remote Sens. Environ. 205, 151–165. https://doi.org/10.1016/j.rse.2017.11.014.

Carder, K.L., Hawes, S.K., Baker, K.A., Smith, R.C., Steward, R.G., Mitchell, B.G., 1991. Reflectance model for quantifying chlorophyll-a in the presence of productivity degradation products. J. Geophys. Res. Atmos. 96 (C11), 20599–20611. https://doi.org/10.1029/91JC02117.

Carlson, C.A., Ducklow, H.W., 1996. Growth of bacterioplankton and consumption of dissolved organic carbon in the Sargasso Sea. Aquat. Microb. Ecol. 10, 69–85. https://doi.org/10.3354/ame010069.

Chen, R.F., Bada, J.L., 1992. The fluorescence of dissolved organic matter in seawater. Mar. Chem. 37, 191–221. https://doi.org/10.1016/0304-4203(92)90078-O.

Chen, J., Lee, Z.P., Hu, C., Wei, J.W., 2016. Improving SeaWiFS data product with a scheme to correct the residual errors in remote sensing reflectance. J. Geophys. Res. Oceans 121, 3866–3886. https://doi.org/10.1002/2016JC011673.

Chen, J., He, X., Zhou, B., Pan, D., 2017. Deriving colored dissolved organic matter absorption coefficient from ocean color with a neural quasi-analytical algorithm. J. Geophys. Res. Oceans 122, 8543–8556. https://doi.org/10.1002/2017JC013115.

Ciotti, A.M., Bricaud, A., 2006. Retrievals of a size parameter for phytoplankton and spectral light absorption by colored detrital matter from water-leaving radiances at SeaWiFS channels in a continental shelf region off Brazil. Limnol. Oceanogr. Methods 4, 237–253. https://doi.org/10.4319/lom.2006.4.237.

Claustre, H., Morel, A., Hooker, S.B., Babin, M., Antoine, D., Oubelkheir, K., et al., 2002. Is desert dust making oligotrophic waters greener? Geophys. Res. Lett. 29 (10), 1469. https://doi.org/10.1029/2001gl014056.

Coble, P.G., 2007. Marine optical biogeochemistry: the chemistry of ocean color. Chem. Rev. 107, 402–418. https://doi.org/10.1021/cr050350+.

Coble, P.G., Del Castillo, C.E., Avril, B., 1998. Distribution and optical properties of CDOM in the Arabian Sea during the 1995 Southwest Monsoon. Deep Sea Res., Pt. II 1998 45, 2195. https://doi.org/10.1016/S0967-0645(98)00068-X.

Coble, P.G., Zepp, R., Zika, R., 2004. CDOM in the ocean: transformation processes and their effects on optical properties. Mar. Chem. 89, 1. https://doi.org/10.1016/j.marchem.2004.06.001.

Del Castillo, C.E., Miller, R.L., 2008. On the use of ocean color remote sensing to measure the transport of dissolved organic carbon by the Mississippi River plume. Remote Sens. Environ. 112 (3), 836–844. https://doi.org/10.1016/j.rse.2007.06.015.

Dutkiewicz, S., Follows, M., Marshall, J., Gregg, W.W., 2001. Interannual variability of phytoplankton abundances in the North Atlantic. Deep Sea Res., Pt. II 48, 2323–2344. https://doi.org/10.1016/S0967-0645(00)00178-8.

Fichot, C., Benner, R., 2011. A novel method to estimate DOC concentrations from CDOM absorption coefficients in coastal waters. Geophys. Res. Lett. 38, L03610 https://doi.org/10.1029/2010GL046152.

Fichot, C., Benner, R., 2012. The spectral slope coefficient of chromophoric dissolved organic matter (S275-295) as a tracer of terrigenous dissolved organic carbon in river-influenced ocean margins. Limnol. Oceanogr. 57 (5), 1453–1466. https://doi.org/10.4319/lo.2012.57.5.1453.

Goyens, C., Jamet, C., Schroeder, T., 2013. Evaluation of four atmospheric correction algorithms for MODIS-aqua images over contrasted coastal waters. Remote Sens. Environ. 131, 63–75. https://doi.org/10.1016/j.rse.2012.12.006.

Hu, C., Lee, Z.P., Muller-Karger, F.E., Carder, K.L., Walsh, J.J., 2006. Ocean color reveals phase shift between marine plants and yellow substance. IEEE Geosci. Remote Sens. Lett. 3 (2), 262–266.

Hu, C., Feng, L., Lee, Z.P., Davis, C.O., Mannino, A., McClain, C.R., Franz, B.A., 2012. Dynamic range and sensitivity requirements of satellite ocean color sensors: learning from the past. Appl. Opt. 51 (25), 6045–6062. https://doi.org/10.1364/AO.51.006045.

Remote sensing of inherent optical properties: Fundamentals, tests of algorithms, and applications. In: IOCCG, Lee, Z.P. (Eds.), 2006. IOCCG Reports, 5. IOCCG, Dartmouth.

Jamet, C., Loisel, H., Dessailly, D., 2012. Retrieval of the spectral diffuse attenuation coefficient $K_d(\lambda)$ in open and coastal ocean waters using a neural network inversion. J. Geophys. Res. Oceans 117, C10023. https://doi.org/10.1029/2012jc008076.

Jorge, D.S.F., Loisel, H., Jamet, C., et al., 2021. A three-step semi analytical algorithm (3SAA) for estimating inherent optical properties over oceanic, coastal, and inland waters from remote sensing reflectance. Remote Sens. Environ. 263, 1–17. https://doi.org/10.1016/j.rse.2021.112537.

Kieber, D.J., Jiao, J., Kiene, R.P., Bates, T.S., 1996. Impact of dimethyl sulfide photochemistry on methyl sulfur cycling in the equatorial Pacific Ocean. J. Geophys. Res. Oceans 101, 3715–3722. https://doi.org/10.1029/95JC03624.

Kopelevich, O.V., Burenkov, V.I., 1977. Relation between the spectral values of the light absorption coefficients of sea water, phytoplanktonic pigments, and the yellow substance. Oceanology 17, 278–282.

Lee, Z.P., Carder, K.L., Arnone, R., 2002. Deriving inherent optical properties from water color: a multi-band quasi-analytical algorithm for optically deep waters. Appl. Opt. 41, 5755–5772. https://doi.org/10.1364/AO.41. 005755.

Lévy, M., Lehahn, Y., André, J.M., Mémery, L., Loisel, H., Heifetz, E., 2005. Production regimes in the northeast Atlantic: A study based on Sea-viewing Wide Field-of-view Sensor (SeaWiFS) chlorophyll and ocean general circulation model mixed layer depth. J. Geophys. Res. Oceans 110, C07S10. https://doi.org/10.1029/2004JC002771.

Loisel, H., Lubac, B., Dessailly, D., Duforet-Gaurier, L., Vantrepotte, V., 2010. Effect of inherent optical properties variability on the chlorophyll retrieval from ocean color remote sensing: an in situ approach. Opt. Express 18, 20949–20952. https://doi.org/10.1364/OE.18.020949.

Loisel, H., Vantrepotte, V., Norkvist, K., Mériaux, X., et al., 2011. Characterization of the bio-optical anomaly and diurnal variability of particulate matter, as seen from scattering and backscattering coefficients, in ultra-oligotrophic eddies of the Mediterranean Sea. Biogeosciences 8 (11), 3295–3317. https://doi.org/10.5194/bgd-8-7859-2011.

Loisel, H., Vantrepotte, V., Dessailly, D., Mériaux, X., 2014. Assessment of the colored dissolved organic matter in coastal waters from ocean color remote sensing. Opt. Express 22 (11), 13109–13124. https://doi.org/10.1364/OE.22.013109.

Loisel, H., Stramski, D., Dessailly, D., Jamet, C., Li, L., Reynolds, R.A., 2018. An inverse model for estimating the optical absorption and backscattering coefficients of seawater from remote-sensing reflectance over a broad range of oceanic and coastal marine environments. J. Geophys. Res. Oceans 123, 2141–2171. https://doi.org/10.1002/2017JC013632.

López, R., Del Castillo, C.E., Miller, R.L., Salisbury, J., Wisser, D., 2012. Examining organic carbon transport by the Orinoco River using SeaWiFS imagery. J. Geophys. Res. Biogeosci. 117, G03022 https://doi.org/10.1029/2012JG001986.

Mannino, A., Russ, M., Hooker, S., 2008. Algorithm development and validation for satellite-derived distributions of DOC and CDOM in the US middle Atlantic bight. J. Geophys. Res. Atmos. 113 (C7), C07051 https://doi.org/10.1029/2007JC004493.

Mannino, A., Novak, M.G., Hooker, S., Hyde, K., Aurin, D., 2014. Algorithm development and validation of CDOM properties for estuarine and continental shelf waters along the northeastern U.S. coast. Remote Sens. Environ. 152, 576–602. https://doi.org/10.1016/j.rse.2014.06.027.

Maritorena, S., Siegel, D.A., 2005. Consistent merging of satellite ocean color data using a semi-analytical model. Remote Sens. Environ. 94, 429–440. https://doi.org/10.1016/j.rse.2004.08.014.

Maritorena, S., Siegel, D.A., Peterson, A.R., 2002. Optimization of a semianalytical ocean color model for global scale applications. Appl. Opt. 41 (15), 2705–2714. https://doi.org/10.1364/AO.41.002705.

Matsuoka, A., Hooker, S.B., Bricaud, A., Gentili, B., Babin, M., 2013. Estimating absorption coefficients of colored chromophoric dissolved organic matter (CDOM) using a semi-analytical algorithm for southern Beaufort Sea waters: application to deriving concentrations of dissolved organic carbon from space. Biogeosciences 10, 917–927. https://doi.org/10.5194/bg-10-917-2013.

Mélin, F., Vantrepotte, V., 2015. How optically diverse is the coastal ocean? Remote Sens. Environ. 160, 235–251. https://doi.org/10.1016/j.rse.2015.01.023.

Mélin, F., Zibordi, G., Berthon, J.F., 2007. Assessment of satellite ocean color products at a coastal site. Remote Sens. Environ. 110 (2), 192–215. https://doi.org/10.1016/j.rse.2007.02.026.

Morel, A., Gentili, B., 2009. A simple band ratio technique to quantify the colored dissolved and detrital organic material from ocean color remotely sensed data. Remote Sens. Environ. 113 (5), 998–1011. https://doi.org/10.1016/j.rse.2009.01.008.

Morel, A., Maritorena, S., 2001. Bio-optical properties of oceanic waters: a reappraisal. J. Geophys. Res. Oceans 106, 7163–7180. https://doi.org/10.1029/2000JC000319.

Morel, A., Huot, Y., Gentili, B., Werdell, P.J., Hooker, S.B., Franz, B.A., 2007. Examining the consistency of products derived from various ocean color sensors in open ocean (case 1) waters in the perspective of a multi-sensor approach. Remote Sens. Environ. 111, 69–88. https://doi.org/10.1016/j.rse.2007.03.012.

Nelson, N.B. and Siegel, D.A., 2002. Chromophoric DOM in the open ocean, Biogeochemistry of Marine Dissolved Organic Matter, D. A. Hansell, C. A. Carslon, Academic.

Nelson, N.B., Siegel, D.A., 2013. The global distribution and dynamics of chromophoric dissolved organic matter. Annu. Rev. Mar. Sci. 2013 (5), 447–476. https://doi.org/10.1146/annurev-marine-120710-100751.

Nelson, N.B., Siegel, D.A., Michaels, A.F., 1998. Seasonal dynamics of colored dissolved organic material in the Sargasso Sea. Deep Sea Res., Pt. I 45, 931–957. https://doi.org/10.1016/S0967-0637(97)00106-4.

Nelson, N.B., Carlson, C.A., Steinberg, D.K., 2004. Production of chromophoric dissolved organic matter by Sargasso Sea microbes. Mar. Chem. 89, 273–287. https://doi.org/10.1016/j.marchem.2004.02.017.

Nelson, N.B., Siegel, D.A., Carlson, C.A., Swan, C., Smethie Jr., W.M., Khatiwala, S., 2007. Hydrography of chromophoric dissolved organic matter in the North Atlantic. Deep-Sea Res. Pt. I 54, 710–731. https://doi.org/10.1016/j.dsr.2007.02.006.

Nelson, N.B., Siegel, D.A., Carlson, C.A., Swan, C.M., 2010. Tracing the global carbon cycle and meridional overturning circulation using chromophoric dissolved organic matter. Geophys. Res. Lett. 37 https://doi.org/10.1029/2009GL042325.

Organelli, E., Bricaud, A., Antoine, D., Matsuoka, A., 2014. Seasonal dynamics of light absorption by chromophoric dissolved organic matter (CDOM) in the NW Mediterranean Sea (BOUSSOLE site). Deep Sea Res. Pt. I 91, 72–85. https://doi.org/10.1016/j.dsr.2014.05.003.

Pahlevan, N., et al., 2021. ACIX-Aqua: a global assessment of atmospheric correction methods for Landsat-8 and Sentinel-2 over lakes, rivers, and coastal waters. Remote Sens. Environ. 258 (2021), 112366. https://doi.org/10.1016/j.rse.2021.112366.

Prieur, L., Sathyendranath, S., 1981. An optical classification of coastal and oceanic waters based on the specific spectral absorption curves of phytoplankton pigments, dissolved organic matter, and other particulate materials. Limnol. Oceanogr. 26, 671–689. https://doi.org/10.4319/lo.1981.26.4.0671.

Raimbault, P., Garcia, N., Cerutti, F., 2008. Distribution of inorganic and organic nutrients in the South Pacific Ocean – evidence for long-term accumulation of organic matter in nitrogen-depleted waters. Biogeosciences 5, 281–298. https://doi.org/10.5194/bgd-4-3041-2007.

Rumelhart, D.E., Hinton, G.E., Willimas, R.J., 1986. Learning internal representations by error propagation. In: Rumelhart, D.E., McClennad, J.L., P. R. Group (Eds.), Parallel Distributed Processing, 1. MIT Press, Cambridge, Mass, pp. 318–6362. https://doi.org/10.7551/mitpress/5236.001.0001.

Salisbury, J., Vandemark, D., Campbell, J., Hunt, C., Wisser, D., Reul, N., Chapron, B., 2011. Spatial and temporal coherence between Amazon River discharge, salinity, and light absorption by colored organic carbon in western tropical Atlantic surface waters. J. Geophys. Res. Oceans 116, C00H02. https://doi.org/10.1029/2011JC006989.

Shanmugam, P., 2011. New models for retrieving and partitioning the colored dissolved organic matter in the global ocean: implications for remote sensing. Remote Sens. Environ. 115, 1501–1521. https://doi.org/10.1016/j.rse.2011.02.009.

Siegel, D.A., Maritorena, S., Nelson, N.B., Hansell, D.A., Lorenzi-Kayser, M., 2002. Global distribution and dynamics of colored dissolved and detrital organic materials. J. Geophys. Res. Oceans 107 (C12), 3228. https://doi.org/10.1029/2001jc000965.

Siegel, D.A., Maritorena, S., Nelson, N.B., Behrenfeld, M.J., 2005a. Independence and interdependencies of global ocean color properties: reassessing the bio-optical assumption. J. Geophys. Res. Atmos. 110 (C07011), 12. https://doi.org/10.1029/2004JC002527.

Siegel, D.A., Maritorena, S., Nelson, N.B., Behrenfeld, M., McClain, C., 2005b. Colored dissolved organic matter and its influence on the satellite-based characterization of the ocean biosphere. Geophys. Res. Lett. 32 (20), L20605 https://doi.org/10.1029/2005GL024310.

Siegel, D.A., Behrenfeld, M., Maritorena, S., McClain, C., Antoine, D., Bailey, S., Bontempi, P., Boss, E., Dierssen, H., Doney, S., 2013. Regional to global assessments of phytoplankton dynamics from the SeaWiFs mission. Remote Sens. Environ. 135, 77–91. https://doi.org/10.1016/j.rse.2013.03.025.

Stedmon, C., Nelson, N.B., 2014. The optical properties of DOM in the ocean. In: Hansell, D.A., Carslon, C.A. (Eds.), Biogeochemistry of Marine Dissolved Organic Matter, 2nd edition.

Swan, C.M., Siegel, D.A., Nelson, N.B., Carlson, C.A., Nasir, E., 2009. Biogeochemical and hydrographic controls on chromophoric dissolved organic matter distribution in the Pacific Ocean. Deep Sea Res., Pt. I 56. https://doi.org/10.1016/j.dsr.2009.09.002.

Swan, C.M., Nelson, N.B., Siegel, D.A., Fields, E.A., 2013. A model for remote estimation of ultraviolet absorption by chromophoric dissolved organic matter based on the global distribution of spectral slope. Remote Sens. Environ. 136, 277–285. https://doi.org/10.1016/j.dsr.2012.01.008.

Toole, D.A., Slezak, D., Kiene, R.P., Kieber, D.J., Siegel, D.A., 2006. Effects of solar radiation on dimethyl sulfide cycling in the western Atlantic Ocean. Deep Sea Res. Pt. I 53, 136–153. https://doi.org/10.1016/j.dsr.2005.09.003.

Tremblay, J.E., Lucas, M.I., Kattner, G., Pollard, R., Strass, V.H., Bathmann, U., Bracher, A., 2002. Significance of the polar frontal zone for large-sized diatoms and new production during summer in the Atlantic sector of the Southern Ocean. Deep Sea Res. Pt. II 49 (18), 3793e3811. https://doi.org/10.1016/S0967-0645(02)00111-X.

Twardowski, M.S., Boss, E., Sullivan, J.M., Donaghay, P.L., 2004. Modeling the spectral shape of absorption by chromophoric dissolved organic matter. Mar. Chem. 89, 69–88. https://doi.org/10.1016/j.marchem.2004.02.008.

Tzortziou, M., Zeri, C., Dimitriou, E., Ding, Y., Jaffe, R., Anagnostou, E., Pitta, E., Mentzafou, A., 2015. Colored dissolved organic matter dynamics and anthropogenic

influences in a major transboundary river and its coastal wetland. Limnol. Oceanogr. 60 (4), 1222–1240. https://doi.org/10.1002/lno.10092.
Vantrepotte, V., Danhiez, F., Loisel, H., Ouillon, S., Mériaux, X., Cauvin, A., 2015. CDOM-DOC relationship in contrasted coastal waters: implication for DOC retrieval from ocean color remote sensing observation. Opt. Express 23 (1), 33–54. https://doi.org/10.1364/OE.23.000033.
Werdell, P.J., Bailey, S.W., 2005. An improved in situ bio-optical data set for ocean color algorithm development and satellite data product validation. Remote Sens. Environ. 98, 122–140. https://doi.org/10.1016/j.rse.2005.07.001.
Zibordi, G., Mélin, F., Berthon, J.F., 2006. A time series of above-water radiometric measurements for coastal water monitoring and remote sensing product validation. IEEE Geosci. Remote Sens. Lett. 3, 120–124. https://doi.org/10.1109/LGRS.2005.858486.